Structural interconversions modulate activity of *Escherichia coli* ribonucleotide reductase

Nozomi Ando[a,b,1], Edward J. Brignole[a,b,c,1], Christina M. Zimanyi[b], Michael A. Funk[b], Kenichi Yokoyama[b], Francisco J. Asturias[c], JoAnne Stubbe[b,d], and Catherine L. Drennan[a,b,d,2]

[a]Howard Hughes Medical Institute, [b]Department of Chemistry, and [d]Department of Biology, Massachusetts Institute of Technology, Cambridge, MA 02139; and [c]Department of Cell Biology, The Scripps Research Institute, La Jolla, CA 92037

Edited by Rowena G. Matthews, University of Michigan, Ann Arbor, MI, and approved October 31, 2011 (received for review August 3, 2011)

Essential for DNA biosynthesis and repair, ribonucleotide reductases (RNRs) convert ribonucleotides to deoxyribonucleotides via radical-based chemistry. Although long known that allosteric regulation of RNR activity is vital for cell health, the molecular basis of this regulation has been enigmatic, largely due to a lack of structural information about how the catalytic subunit (α_2) and the radical-generation subunit (β_2) interact. Here we present the first structure of a complex between α_2 and β_2 subunits for the prototypic RNR from *Escherichia coli*. Using four techniques (small-angle X-ray scattering, X-ray crystallography, electron microscopy, and analytical ultracentrifugation), we describe an unprecedented $\alpha_4\beta_4$ ring-like structure in the presence of the negative activity effector dATP and provide structural support for an active $\alpha_2\beta_2$ configuration. We demonstrate that, under physiological conditions, *E. coli* RNR exists as a mixture of transient $\alpha_2\beta_2$ and $\alpha_4\beta_4$ species whose distributions are modulated by allosteric effectors. We further show that this interconversion between $\alpha_2\beta_2$ and $\alpha_4\beta_4$ entails dramatic subunit rearrangements, providing a stunning molecular explanation for the allosteric regulation of RNR activity in *E. coli*.

allostery | protein–protein interactions | conformational equilibria | nucleotide metabolism

Important targets of anticancer and antiviral drugs, ribonucleotide reductases (RNRs) are classified by the metallocofactor used to generate a thiyl radical (1) that initiates reduction of ribonucleotides to deoxyribonucleotides (2, 3). Class Ia RNRs are found in all eukaryotes and many aerobic bacteria, with the *Escherichia coli* enzyme serving as the prototype. These RNRs reduce ribonucleoside 5′-diphosphates and are composed of two homodimeric subunits: α_2 and β_2 (Fig. 1*A*). The α_2 subunit contains the active site, where ribonucleotide reduction occurs, and two types of allosteric effector binding sites (4, 5). One effector site tunes the specificity for all four ribonucleotide substrates in response to intracellular levels of deoxyribonucleoside 5′-triphosphates (dATP, dTTP, dGTP) and ATP (6, 7) such that balanced pools of deoxyribonucleotides are maintained (8). The second effector site controls the rate of reduction, binding ATP to turn the enzyme on or dATP to turn it off (4, 6). This activity site is housed in an N-terminal cone domain (5, 9) and provides a means for negative feedback regulation to safeguard against cytotoxic elevation of deoxyribonucleotide levels (2, 3, 10). The β_2 subunit harbors the essential diferric-tyrosyl radical (Y122• in *E. coli*) cofactor (11) that initiates radical chemistry.

Active RNR has long been proposed to be a transient $\alpha_2\beta_2$ complex (Fig. 1*B*) with enhanced subunit affinity upon binding of substrates and effectors (12–15). For each turnover, α_2, β_2, substrate and effector must interact, triggering long-range proton-coupled electron transfer (PCET) reducing Y122• in β_2 and oxidizing C439 to a thiyl radical in the active site of α_2, over an unprecedented distance of >35 Å (13, 15, 16) (Fig. 1*C*). Once the thiyl radical is generated in the active site of α_2, ribonucleotide reduction proceeds through a conserved mechanism (17). Allosteric regulation of this activity is key to cell survival and involves conformational changes as well as oligomeric state changes in both prokaryotic (12, 14, 18) and eukaryotic systems (19–23). For *E. coli* (12, 14, 18), mouse (20–22), yeast (19), and human (19, 23), the negative effector dATP has been linked to increases in oligomeric state with a recent gas-phase electrophoretic molecular mobility analysis (GEMMA) study estimating a molecular mass of 510 kDa for the dATP-inhibited *E. coli* RNR (most consistent with an $\alpha_4\beta_4$ state) (18), whereas for human and yeast RNR, dATP has been linked to α-hexamerization (19, 22, 23).

To understand the role of oligomeric state in the activity regulation of this prototypic class Ia RNR from *E. coli*, we have combined data from four complementary structural techniques. Using small-angle X-ray scattering (SAXS) and analytical ultracentrifugation (AUC), we provide evidence that supports a compact $\alpha_2\beta_2$ structure for the active complex that can be reversibly converted via a dynamic conformational rearrangement to an inactive $\alpha_4\beta_4$ state in the presence of elevated dATP or protein concentrations. Additionally, using SAXS, single-particle EM, and X-ray crystallography, we demonstrate that the $\alpha_4\beta_4$ complex induced by the negative effector, dATP, is an unexpected ring-like structure composed of alternating α_2 and β_2 subunits. Together, these results explain how activity can be modulated by oligomerization, which is induced by effector binding at an allosteric site that is approximately 42 Å from the active site.

Results

dATP Shifts Oligomeric Equilibrium. Sedimentation velocity AUC was employed to investigate the oligomeric distributions of *E. coli* RNR at multiple protein concentrations and in the presence of effectors at physiologically relevant concentrations (approximately 175 μM for dATP, 3 mM for ATP, and 0.1 mM for dTTP) (24–27). Using β_2 that was pretreated with hydroxyurea to prevent turnover and thus oxidation of the active site during measurements, three different modes of RNR regulation were investigated: (*i*) under negative feedback regulation with dATP in both specificity and activity sites and CDP as the substrate; (*ii*) under enhanced CDP reduction with ATP in both specificity and activity sites and CDP as the substrate; and (*iii*) under GDP reduction with dTTP in the specificity site and no effector in the activity site.

Author contributions: N.A., E.J.B., C.M.Z., F.J.A., J.S., and C.L.D. designed research; N.A. performed SAXS and AUC experiments and data analysis; E.J.B. performed EM experiments and image analysis; C.M.Z. performed crystallization and crystal structure determination; M.A.F. and K.Y. prepared samples and performed AUC and SAXS experiments; and N.A., E.J.B., J.S., and C.L.D. wrote the paper.

The authors declare no conflict of interest.

This article is a PNAS Direct Submission.

Freely available online through the PNAS open access option.

Data deposition: The atomic coordinates and structure factors have been deposited in the Protein Data Bank, www.pdb.org (PDB ID code 3UUS).

[1]N.A. and E.J.B. contributed equally to this work.

[2]To whom correspondence should be addressed. E-mail: cdrennan@mit.edu.

This article contains supporting information online at www.pnas.org/lookup/suppl/doi:10.1073/pnas.1112715108/-/DCSupplemental.

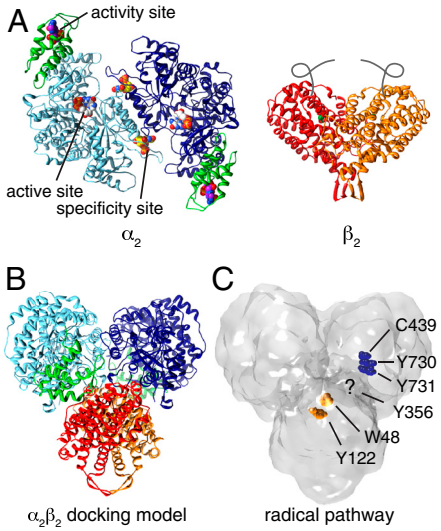

Fig. 1. Previously determined structures and proposed models for *E. coli* class Ia RNR. (*A*) Homodimeric α_2 with nucleotides bound (spheres) and the cone domains (residues 1–100) colored in green. Homodimeric β_2 with diiron centers (green) and disordered C termini (gray lines). Protein Data Bank ID codes 4R1R, 3R1R, 1RIB (5, 15, 28). (*B*) Proposed $\alpha_2\beta_2$ model in which the subunits are docked along their symmetry axis (15). (*C*) Docking model rendered as a surface. Radical pathway involving Y122 → W48 → Y356 in β_2 (Y122 and W48 shown as orange spheres) and residues Y731 → Y730 → C439 in α_2 (dark-blue spheres). Y356 in β_2 lies in the disordered C termini (15).

In the presence of saturating dATP and CDP, α_2 alone and β_2 alone sediment at 5.2 and 8.4 S, respectively (Fig. 2*A*). These sedimentation coefficients are in good agreement with previously reported experimental values (12, 14) as well as theoretical values calculated from their crystal structures (5, 28) of 5.8 and 8.4 S. Similar results are obtained for the individual subunits with ATP/CDP and dTTP/GDP (*SI Appendix*, Fig. S1). When α_2 and β_2 are combined in the presence of saturating dATP/CDP, a distinct peak is observed at 15.6 S at a physiological RNR concentration of 1 μM (26, 27) (Fig. 2*A*). Increasing the protein concentration does not result in peak shifts, indicating that the 15.6-S peak can be attributed to a single slowly dissociating species (29). Gaussian fitting to the peak yields a molecular mass of 533 kDa by the Svedberg relation (30) (*SI Appendix*, Fig. S2), similar to the 510-kDa estimate for the dATP-inhibited *E. coli* enzyme reported by GEMMA (18), and consistent with an $\alpha_4\beta_4$ complex. A typical globular protein of this molecular mass has a frictional ratio of 1.2, giving an expected sedimentation coefficient of 19 S (31). This value is much larger than the observed value for the dATP-inhibited complex, suggesting that this complex is highly nonglobular.

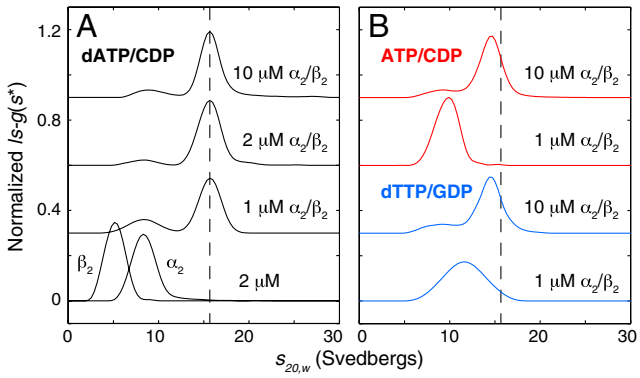

Fig. 2. Sedimentation coefficient distributions of *E. coli* class Ia RNR: dATP and high protein concentrations shift the equilibrium toward a large complex. Physiologically relevant effector and substrate concentrations were chosen to saturate their respective sites, based on previously reported nucleotide-binding affinities (4, 24, 25, 34, 51). (*A*) In the presence of 175 μM dATP and 1 mM CDP, the individual subunits (each at 2 μM) sediment at 5.2 and 8.4 S. When mixed, a single slowly dissociating 15.6 S complex is observed with a molecular mass of 533 kDa. (*B*) In the presence of 3 mM ATP and 1 mM CDP (red curves) or 0.1 mM dTTP and 1 mM GDP (blue curves), broad, protein concentration-dependent peaks are observed, indicative of multiple species in rapid exchange. Raising the protein concentration leads to a peak shift toward 15.6 S (position indicated by dashed line). Curves are offset by a constant value for clarity.

In contrast, broad peaks with maxima near 10–11.5 S were observed in the presence of saturating dTTP/GDP or ATP/CDP at 1 μM protein concentration (Fig. 2*B*). Gaussian fitting of these peaks did not yield molecular mass estimates that were consistent with any one single species of RNR, including the expected $\alpha_2\beta_2$ active complex. Furthermore, increasing the protein concentration by 10-fold shifted the dominant peak toward 15.6 S (dashed line in Fig. 2*B*), approaching the sedimentation coefficient of the dATP-inhibited complex. The observation of broad peaks that shift with increasing protein concentration is the hallmark of a mixture of rapidly exchanging species rather than a single species (29). Contrary to our previous understanding of *E. coli* class Ia RNR, the peak shifts observed here indicate that a large complex dominates at high protein concentration in the absence of dATP, with no effector in the activity site (Fig. 2*B*, dTTP/GDP) or even with a positive activity regulator occupying the activity site (Fig. 2*B*, ATP/CDP). Significantly, the peak shifts suggest that, under these conditions, this large complex is able to rapidly exchange with smaller species and is therefore in the equilibrium mixture even at physiological protein concentrations.

dATP-Inhibited Complex Contains Both α_2 and β_2. To determine the subunit composition and stoichiometry of the dATP-inhibited complex, we used SAXS, a structural technique that provides protein size and shape information in solution. α_2 was titrated into β_2 under identical dATP/CDP conditions investigated by AUC, leading to a rapid and dramatic increase in radius of gyration (R_g) up to the equimolar point, consistent with the formation of a large complex with 1:1 subunit stoichiometry (*SI Appendix*, Fig. S3). Given the 533-kDa molecular mass determined by AUC, a 1:1 complex is most consistent with a 517 kDa $\alpha_4\beta_4$ oligomerization state.

As a control, α_2 was examined under identical conditions without β_2. The R_g of α_2 alone showed minimal concentration dependence with a value of 39.7 ± 0.3 Å when extrapolated to zero protein concentration to eliminate the effects of interparticle interactions (*SI Appendix*, Fig. S3*B*), in excellent agreement with the theoretical value of 39.3 Å calculated from the α_2 crystal structure (5). The reverse titration and corresponding control with β_2 alone yielded similar results (*SI Appendix*, Fig. S4), showing that both α_2 and β_2 must be present for the formation of higher order oligomers.

Structure of the dATP-Inhibited Complex Is an $\alpha_4\beta_4$ Ring. EM and X-ray crystallography were used to investigate the architecture of the dATP-induced $\alpha_4\beta_4$ complex. EM images were acquired of 0.15 μM α_2 and β_2 in the presence of 1 mM CDP and 0, 1, or 50 μM dATP (Fig. 3*A* and *SI Appendix*, Fig. S5). In the absence of dATP, the subunits are largely dissociated, as expected from the measured micromolar subunit affinity (32). The addition of dATP drives the formation of distinct ring-like complexes approximately 200 Å in outer diameter. Images of these ring-shaped particles were aligned and classified (*SI Appendix*, Fig. S6) and the resulting class averages are consistent with α_2 and β_2 subunits arranged in an alternating pattern, forming an $\alpha_4\beta_4$ complex (Fig. 3*B*, Average). Because the EM images were collected as tilted–untilted pairs, we were able to generate a 3D

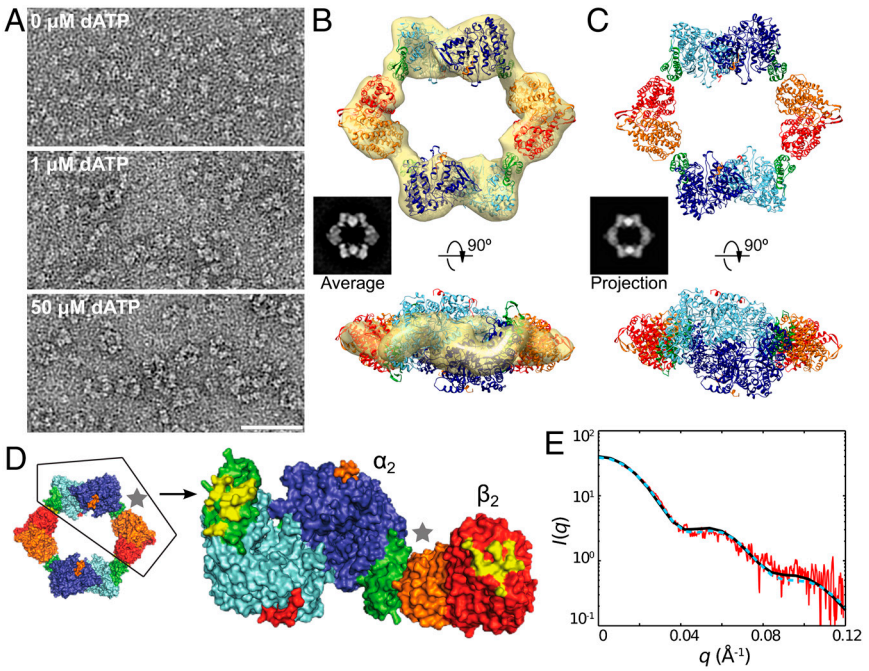

Fig. 3. Structure of the dATP $\alpha_4\beta_4$ complex by EM and X-ray crystallography. (*A*) EM images of RNR in the presence of 1 mM CDP and increasing dATP concentrations show the formation of $\alpha_4\beta_4$ rings. (*B*) A class average with 1039 particles (Average) is representative of the ring structures observed at 50 μM dATP and is composed of alternating α_2 and β_2 subunits as indicated by its close resemblance to the 2D projection of the $\alpha_4\beta_4$ crystal structure (Projection in *C*). These insets are 314-Å wide. Crystal structures of individual α_2 and β_2 subunits (5, 39), colored as in Fig. 1, fit to a 3D EM map of the $\alpha_4\beta_4$ ring structure. (*C*) Crystal structure of dATP-bound RNR at 5.65-Å resolution with the asymmetric unit containing an $\alpha_4\beta_4$ ring that agrees well with the EM model (5–9 Å C^α rmsd). (*D*) Surface rendering of the crystal structure with half of the ring removed, revealing the areas on α and β that are buried (yellow) upon formation of the $\alpha_4\beta_4$ ring. (*E*) Experimental solution scattering (red) of 2 μM RNR in the presence of saturating dATP/CDP superimposed with the theoretical scattering curves calculated from the EM model (black solid) and crystal structure (cyan dashed).

map of the $\alpha_4\beta_4$ ring at approximately 23-Å resolution (Fig. 3*B* and *SI Appendix*, Fig. S7). Crystal structures of the individual dimeric subunits (5, 28) could be unambiguously fit to the 3D map of the $\alpha_4\beta_4$ ring, confirming the alternating subunit arrangement suggested by the 2D class averages.

To obtain a more detailed picture of the $\alpha_4\beta_4$ complex, a 5.65-Å resolution crystal structure was obtained by cocrystallizing α_2 and β_2 with 10 mM dATP (Fig. 3*C* and *SI Appendix*, Table S1). The structure, which was solved by molecular replacement, displays electron density for dATP bound at both activity and specificity sites (*SI Appendix*, Fig. S8 *D* and *E*) and reveals the same $\alpha_4\beta_4$ ring-shaped species in the asymmetric unit of the crystal as that observed by EM (Fig. 3 *B* and *C*). The individual α_2 and β_2 subunits of the $\alpha_4\beta_4$ structure align well with structures of uncomplexed α_2 and β_2 subunits, showing only small variations in the α_2 cone domain, and sharing overall average root-mean-square derivations of 1.11 and 1.01 Å for α_2 and β_2 subunits, respectively (*SI Appendix*, Fig. S8 *B* and *C*). In the $\alpha_4\beta_4$ structure, α_2 and β_2 contact each other at two points. In addition to the previously identified (15) binding pocket on α_2 for the C terminus of β_2, we find a second interaction between the activity site, housed in the N-terminal cone domain of α_2 (Fig. 3 *C* and *D*, green), and each lobe of β_2 (Fig. 3 *C* and *D*, red/orange). This direct contact between the dATP-bound α_2 activity site and the β_2 subunits provides a molecular explanation for how the presence of activity effectors can be sensed, leading to the regulation of activity. From these structural data, we can also rationalize why a dATP-induced $\alpha_4\beta_4$ complex would be inactive. We find that residues on the radical propagation pathway (Fig. 1*C*) are not aligned appropriately for electron transfer, instead facing a large central opening approximately 100 Å in diameter (Fig. 3*C*) such that W48 of β_2 and Y731 of α_2 are solvent exposed, and Y356 on the flexible C-terminal tail of β_2 remains disordered. Also, the distance between W48 and Y731 is too long (*ca.* 55–58 Å) for PCET via only a single residue in the middle (Y356). In contrast, for active *E. coli* RNR, expected W48-Y731 distances are approximately 23–25 Å based on the proposed docking model (15) (Fig. 1*B*), which has been supported experimentally using distance restraints from pulsed electron–electron double resonance (PELDOR) spectroscopy (13).

The unanticipated $\alpha_4\beta_4$ structure observed by EM and crystallography is supported by SAXS and AUC. Importantly, the use of these four methods allows for the interrogation of this RNR structure at a wide range of protein and dATP concentrations. Protein concentrations of 0.15 μM (EM) to 25 μM (X-ray), and dATP concentrations of 50 μM (EM) to 10 mM (X-ray) were examined. In addition, physiological concentrations of protein (1–2 μM) and dATP (175 μM) were investigated by AUC and SAXS in solution. Over this wide range of conditions, we find a consistent view of the $\alpha_4\beta_4$ structure. The theoretical sedimentation coefficient calculated from the $\alpha_4\beta_4$ structure is 15.6 S, in excellent agreement with that observed experimentally by AUC (Fig. 2*A*). The extrapolated R_g of 71.1 ± 1.1 Å for $\alpha_4\beta_4$ determined by SAXS (*SI Appendix*, Fig. S9) is a larger value than expected for a globular protein of this molecular mass, but consistent with an open ring structure. Moreover, theoretical scattering curves calculated from the $\alpha_4\beta_4$ X-ray and EM structures agree well with the experimental scattering obtained by SAXS (Fig. 3*E*), demonstrating that the $\alpha_4\beta_4$ ring is not only stable in solution, but also the dominant form of the complex under negative feedback regulation by dATP near physiological protein and effector concentrations.

dATP Promotes Subunit Rearrangement. With the structures of free α_2 and β_2 determined previously (5, 28) and the structure of the dATP-inhibited $\alpha_4\beta_4$ complex now determined by both EM and crystallography, SAXS was used to study the interconversion between different oligomeric states in solution. SAXS is ideal

for probing structural interconversions as the relative fractions of individual states can be deconvoluted from mixtures (33). Titration of dATP into RNR in the presence of CDP leads to a dramatic change in the shape of the scattering curves and their corresponding Kratky curves, indicative of a transition from a predominantly compact state to a nonglobular state (Fig. 4 *A* and *B*). Above 24 μM dATP, or 4 molar equivalents of dATP per α_2, the scattering curves are nearly superimposable and the R_g approaches that of the $\alpha_4\beta_4$ ring (*SI Appendix*, Fig. S10). This result is consistent with full dATP occupancy in the effector sites of $\alpha_4\beta_4$, as expected from the reported dATP binding affinities for the specificity and activity sites of 0.5 and 5 μM, respectively (4, 34).

Isointensity points in the scattering curves are observed, indicating that this structural change can be explained by a two-state process (35) (Fig. 4*A*). Consistent with this interpretation, singular value decomposition shows that the scattering curves can be fit to linear combinations of two independent states with low residuals (*SI Appendix*, Fig. S11). The two-state transition is accompanied by an increase in the zero-angle scattering intensity $I(0)$, which is a function of protein concentration and the electron density contrast between the hydrated protein and buffer (36). Because the protein concentration was fixed and the micromolar dATP concentration does not significantly affect the buffer density, the large increase in $I(0)$ can only be explained by an increase in protein mass. Using experimental $I(0)$ values from the individual subunits as calibrants, the average molecular mass in the dATP-driven transition was calculated to increase from 223 kDa in the absence of dATP to 512 kDa at saturating dATP (*SI Appendix*, Fig. S12). These values are in close agreement with the 259 kDa $\alpha_2\beta_2$ expected in the absence of dATP and the 517 kDa $\alpha_4\beta_4$ expected under saturating dATP. The excellent molecular mass estimation of $\alpha_4\beta_4$ by this method suggests that the subunits have similar excluded volumes, and hence similar hydration layers, as the free subunits (37). In contrast, the underestimation in molecular mass of $\alpha_2\beta_2$ can be at least in part explained by diminished hydration around the individual subunits due to the compact arrangement as determined by Kratky analysis (Fig. 4*B*).

An ab initio shape reconstruction was performed on the scattering curve measured in the absence of dATP, yielding a globular, three-lobed molecular envelope (Fig. 4*D*, *Center*). Consistent with the molecular mass estimation and compact shape, this molecular envelope aligns well with the proposed $\alpha_2\beta_2$ "docking" model for active RNR (15). The fractions of this compact $\alpha_2\beta_2$ and of $\alpha_4\beta_4$ in the dATP titration series were determined (Fig. 4*C*) from a two-state fit to the scattering curves with low residuals (*SI Appendix*, Fig. S13*B*). By comparison, poor fits were obtained with open configurations of $\alpha_2\beta_2$, including an arrangement based on the previously reported asymmetric structure of a class Ib RNR from *Salmonella typhimurium* (38) (*SI Appendix*, Fig. S13*C*). Together, these results indicate that the addition of dATP drives a two-state transition from a compact state, in which the subunits are closely associated, to that in which the subunits form an open ring (Fig. 4 *C* and *D*, and *SI Appendix*, Fig. S10).

Discussion

Allosteric regulation of activity in class Ia RNR provides a mechanism to prevent the accumulation of cytotoxic levels of deoxyribonucleotides. dATP is unique among allosteric effectors in its ability to down-regulate RNR activity (4, 6). Here, using SAXS, EM, and X-ray crystallography, we present a structural model to explain dATP inhibition of activity for the prototypic class Ia RNR. We find that the dATP-inhibited complex has an $\alpha_4\beta_4$ stoichiometry as predicted by GEMMA (18), but with an unprecedented arrangement of alternating subunits in an open ring structure. Importantly, we have confirmed this surprising structure using four different techniques and have shown that this state is the predominant species stabilized by dATP under physiological solution conditions. Using the same concentration of protein in the absence of dATP, the SAXS data agree well with the predicted $\alpha_2\beta_2$ docking model of the active RNR (15), providing a structural depiction of the elusive $\alpha_2\beta_2$ oligomerization state.

In addition to high dATP concentrations driving the formation of the $\alpha_4\beta_4$ state of *E. coli* RNR, AUC results show that increasing protein concentrations also shift the conformational equilibrium toward the higher molecular mass $\alpha_4\beta_4$ (Fig. 2*B*). At lower protein concentrations and in the absence of dATP, $\alpha_4\beta_4$ is still present but to a smaller degree, in rapid equilibrium with the active $\alpha_2\beta_2$ state. Taken together, the SAXS and AUC results suggest that the active RNR complex is an intermediate between two inactive states, the dissociated α_2 and β_2 and the $\alpha_4\beta_4$ ring (Fig. 4*D*),

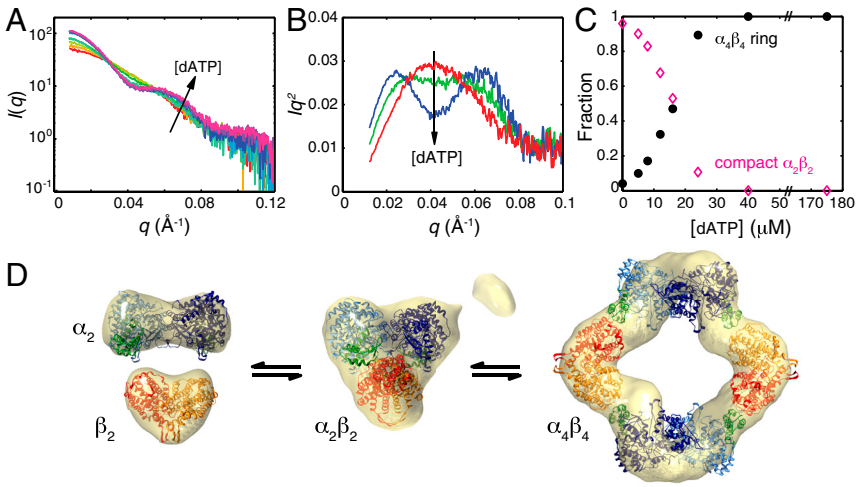

Fig. 4. SAXS investigation of the transition between lower and higher order structures of *E. coli* class Ia RNR. (*A*) Scattering curves measured as 0–175 μM dATP was titrated into a 6 μM solution of α_2 and β_2 in the presence of 1 mM CDP (red to violet) display isointensity points, suggesting a two-state transition. (*B*) Kratky representations of the scattering curves (Iq^2 vs. q) at 0 μM (red), 12 μM (green), and 40 μM (blue) dATP show a transition from a compact globular state, as indicated by the monomodal peak, to a large nonglobular state, indicated by a bimodal curve (36). (*C*) Fitting linear combinations of the $\alpha_2\beta_2$ docking model (15) and the $\alpha_4\beta_4$ ring to the titration data provided relative fractions of the two states. (*D*) Ab initio SAXS reconstructions of free subunits aligned with deposited crystal structures (5, 39), a compact $\alpha_2\beta_2$ state aligned with the proposed docking model (15), and the $\alpha_4\beta_4$ ring aligned with the crystal structure (*SI Appendix*, Tables S2 and S3, and Fig. S10). The small additional density observed in the molecular envelope of $\alpha_2\beta_2$ can be explained by the presence of approximately 3% $\alpha_4\beta_4$ (Fig. 4*C*).

and that the equilibrium between these states is sensitive to both protein and effector concentrations.

Although it has long been known that the α_2 cone domain binds the activity effectors ATP and dATP (5, 19), this $\alpha_4\beta_4$ structure provides a molecular explanation for how the cone domain regulates the activity of *E. coli* RNR. We find that each α_2 cone domain contacts a lobe of β_2, burying a surface area (556 Å^2 at each of four interfaces; Fig. 3*D*) that is large enough to stabilize the ring structure as the dominant species under physiologically relevant protein (1–2 μM) and dATP (175 μM) concentrations in the absence of ATP, although not so large as to inhibit interconversion back to the active $\alpha_2\beta_2$ state in the presence of ATP and other effectors. In the $\alpha_4\beta_4$ state, the radical transfer pathway from β_2 to α_2 is disrupted and solvent exposed, unable to propagate radicals. In contrast, in a compact $\alpha_2\beta_2$ state, these residues are expected to be closer together, buried, and shielded from bulk water (15). Thus the cone domain of α_2 "communicates" the nucleotide levels of the cell to β_2, and the equilibrium of conformers can be shifted toward the $\alpha_4\beta_4$ state, disrupting the radical pathway and inhibiting activity, or toward $\alpha_2\beta_2$, restoring the radical pathway and enzyme activity, as nucleotide levels dictate.

Interestingly, a recently published 6.6-Å structure of yeast RNR also shows the α_2 cone domain to be present at a protein–protein interface. In this case, however, the interface connects two α-subunits in a dATP-induced α_6 hexamer (19). Although it is still early in terms of understanding structure/function for eukaryotic RNRs, this recent structural work along with the results presented here provide compelling support for the involvement of the cone domain in the formation of high-order RNR oligomers and pave the way for future studies.

Twenty-one years after the structure of β_2 was published (39), a structure of an αβ-complex for this prototypic class Ia RNR is now available. Through the power of multiple structural techniques and combined efforts of multiple laboratories, the structures of all dominant forms of this enzyme can now be described. From crystallography and SAXS, views of the dissociated subunits are available (this work and refs. 5 and 28), from SAXS and PELDOR, low-resolution structural data support an active $\alpha_2\beta_2$ model (this work and ref. 13), and from crystallography, EM, and SAXS, the structure of an allosterically inhibited $\alpha_4\beta_4$ ring has been determined (this work). These structures have broad applications, providing a molecular framework for considering the relationship between in vivo *E. coli* nucleotide concentrations and RNR activity, as well as offering a basis for the rational design of a class of inhibitors that could act by stabilizing inactive oligomeric states of the enzyme. This open ring structure of alternating subunits is the latest surprise as this prototypic RNR enzyme, in all of its states, comes into focus.

Materials and Methods

E. coli α_2 and β_2 were isolated as previously described (40, 41). All of the β_2 used in these structural studies was treated with hydroxyurea (HU) to reduce the essential tyrosyl radical to prevent substrate turnover. All experiments were performed in the standard assay buffer (50 mM Hepes, pH 7.6, 15 mM $MgCl_2$ 1 mM EDTA) with 5 mM DTT and the nucleotide concentrations adjusted to the indicated levels.

Crystallization of α_2 and β_2 with dATP was performed by hanging drop vapor diffusion at pH 7.5. Data were collected at the Advanced Light Source beamline 8.2.2, and the structure was solved by molecular replacement using the coordinates 2R1R (5) and 1MXR (42) to 5.65-Å resolution and *R* factors of 25.7 (work) and 30.3 (free) (*SI Appendix*, Table S1).

SAXS images were collected at the Cornell High Energy Synchrotron Source G1 station and processed following previously described protocols (43). Data analyses were performed using the ATSAS package (44) and MATLAB (MathWorks). The momentum transfer variable, *q*, is defined as $q = 4\pi/\lambda \sin\theta$, where 2θ is the scattering angle, and λ is the X-ray wavelength.

Sedimentation velocity AUC was performed using a Beckman XL-I analytical ultracentrifuge equipped with interference optics. Sedimentation coefficient distributions $g(s^*)$ and $ls\text{-}g^*(s)$ were generated in DCDT+ (30) and Sedfit (45), respectively. The *s* values were corrected to standard values ($s_{20,w}$) using Sednterp (46). Theoretical $s_{20,w}$ values were calculated with HYDROPRO (47).

EM specimens were prepared by staining with uranyl acetate. Eighty-nine pairs of CCD images of untilted and −55° tilted specimens were collected on a Tecnai F20 electron microscope (FEI). Particles were selected in untilted images using e2boxer.py (48) and were matched with particles from tilted images using TiltPicker (49). A final dataset of 13,895 untilted particles were iteratively aligned and classified using SPIDER as described previously (50) and the corresponding set of tilted images used to generate a 3D reconstruction for each class.

ACKNOWLEDGMENTS. We thank Deborah Pheasant [Massachusetts Institute of Technology (MIT) Biophysical Instrumentation Facility] and Dr. Walter Stafford (Boston Biomedical Research Institute) for helpful discussions on AUC. For assistance with SAXS data collection, we thank Mackenzie Firer-Sherwood (Boston University), Yan Kung (MIT), and Cornell High Energy Synchrotron Source (CHESS) scientists, Drs. Arthur Woll and Richard Gillilan. We thank Prof. Sol Gruner (Cornell) for access to SAXS equipment and wet lab space. CHESS is supported by the National Science Foundation (NSF) and National Institutes of Health/National Institute of General Medical Sciences (NIH/NIGMS) via NSF award DMR-0936384, and the Macromolecular Diffraction Facility at CHESS resource is supported by NIH/National Center for Research Resources (NCRR) award RR-01646. Electron microscopy was performed at the National Resource for Automated Molecular Microscopy, which is supported by the NIH though the NCRR P41 program (RR017573). Crystallographic data collection was conducted at Advanced Light Source, a Department of Energy (DOE) national user facility (Contract DE-AC02-05CH11231), at beamline 8.2.2 operated by the Berkeley Center for Structural Biology, which is supported in part by the DOE and NIH/NIGMS. This work was supported by NIH grants F32GM904862 (to N.A.), F32DK080622 (to E.J.B.), T32GM08334 (to C.M.Z.), GM67167 (to F.J.A.), and GM29595 (to J.S.), and the NSF Graduate Research Fellowship under Grant 0645960 (to M.A.F.). C.L.D. is a Howard Hughes Medical Institute Investigator.

1. Licht S, Gerfen GJ, Stubbe J (1996) Thiyl radicals in ribonucleotide reductases. *Science* 271:477–481.
2. Jordan A, Reichard P (1998) Ribonucleotide reductases. *Annu Rev Biochem* 67:71–98.
3. Nordlund P, Reichard P (2006) Ribonucleotide reductases. *Annu Rev Biochem* 75:681–706.
4. Brown NC, Reichard P (1969) Role of effector binding in allosteric control of ribonucleoside diphosphate reductase. *J Mol Biol* 46:39–55.
5. Eriksson M, et al. (1997) Binding of allosteric effectors to ribonucleotide reductase protein R1: Reduction of active-site cysteines promotes substrate binding. *Structure* 5:1077–1092.
6. Larsson A, Reichard P (1966) Enzymatic synthesis of deoxyribonucleotides. IX. Allosteric effects in the reduction of pyrimidine ribonucleotides by the ribonucleoside diphosphate reductase system of Escherichia coli. *J Biol Chem* 241:2533–2539.
7. Larsson A, Reichard P (1966) Enzymatic synthesis of deoxyribonucleotides. X. Reduction of purine ribonucleotides; allosteric behavior and substrate specificity of the enzyme system from Escherichia coli B. *J Biol Chem* 241:2540–2549.
8. Reichard P (1988) Interactions between deoxyribonucleotide and DNA synthesis. *Annu Rev Biochem* 57:349–374.
9. Aravind L, Wolf YI, Koonin EV (2000) The ATP-cone: An evolutionarily mobile, ATP-binding regulatory domain. *J Mol Microbiol Biotechnol* 2:191–194.
10. Wheeler LJ, Rajagopal I, Mathews CK (2005) Stimulation of mutagenesis by proportional deoxyribonucleoside triphosphate accumulation in Escherichia coli. *DNA Repair (Amst)* 4:1450–1456.
11. Sjöberg B-M, Reichard P (1977) Nature of the free radical in ribonucleotide reductase from Escherichia coli. *J Biol Chem* 252:536–541.
12. Brown NC, Reichard P (1969) Ribonucleoside diphosphate reductase. Formation of active and inactive complexes of proteins B1 and B2. *J Mol Biol* 46:25–38.
13. Seyedsayamdost MR, Chan CT, Mugnaini V, Stubbe J, Bennati M (2007) PELDOR spectroscopy with DOPA-beta2 and NH2Y-alpha2s: Distance measurements between residues involved in the radical propagation pathway of E. coli ribonucleotide reductase. *J Am Chem Soc* 129:15748–15749.
14. Thelander L (1973) Physicochemical characterization of ribonucleoside diphosphate reductase from Escherichia coli. *J Biol Chem* 248:4591–4601.
15. Uhlin U, Eklund H (1994) Structure of ribonucleotide reductase protein R1. *Nature* 370:533–539.
16. Reece SY, Hodgkiss JM, Stubbe J, Nocera DG (2006) Proton-coupled electron transfer: The mechanistic underpinning for radical transport and catalysis in biology. *Philos Trans R Soc Lond B Biol Sci* 361:1351–1364.
17. Stubbe J (1998) Ribonucleotide reductases in the twenty-first century. *Proc Natl Acad Sci USA* 95:2723–2724.
18. Rofougaran R, Crona M, Vodnala M, Sjöberg B-M, Hofer A (2008) Oligomerization status directs overall activity regulation of the Escherichia coli class Ia ribonucleotide reductase. *J Biol Chem* 283:35310–35318.
19. Fairman JW, et al. (2011) Structural basis for allosteric regulation of human ribonucleotide reductase by nucleotide-induced oligomerization. *Nat Struct Mol Biol* 18:316–322.

20. Kashlan OB, Cooperman BS (2003) Comprehensive model for allosteric regulation of mammalian ribonucleotide reductase: Refinements and consequences. *Biochemistry* 42:1696–1706.
21. Kashlan OB, Scott CP, Lear JD, Cooperman BS (2002) A comprehensive model for the allosteric regulation of mammalian ribonucleotide reductase. Functional consequences of ATP- and dATP-induced oligomerization of the large subunit. *Biochemistry* 41:462–474.
22. Rofougaran R, Vodnala M, Hofer A (2006) Enzymatically active mammalian ribonucleotide reductase exists primarily as an alpha6beta2 octamer. *J Biol Chem* 281:27705–27711.
23. Wang J, Lohman GJ, Stubbe J (2007) Enhanced subunit interactions with gemcitabine-5′-diphosphate inhibit ribonucleotide reductases. *Proc Natl Acad Sci USA* 104:14324–14329.
24. Bochner BR, Ames BN (1982) Complete analysis of cellular nucleotides by two-dimensional thin layer chromatography. *J Biol Chem* 257:9759–9769.
25. Buckstein MH, He J, Rubin H (2008) Characterization of nucleotide pools as a function of physiological state in Escherichia coli. *J Bacteriol* 190:718–726.
26. Eriksson S, Sjöberg B-M, Hahne S (1977) Ribonucleoside diphosphate reductase from Escherichia coli. An immunological assay and a novel purification from an overproducing strain lysogenic for phage lambdadnrd. *J Biol Chem* 252:6132–6138.
27. Hristova D, Wu CH, Jiang W, Krebs C, Stubbe J (2008) Importance of the maintenance pathway in the regulation of the activity of Escherichia coli ribonucleotide reductase. *Biochemistry* 47:3989–3999.
28. Nordlund P, Eklund H (1993) Structure and function of the Escherichia coli ribonucleotide reductase protein R2. *J Mol Biol* 232:123–164.
29. Stafford WF (2009) Protein-protein and ligand-protein interations studied by analytical ultracentrifugation. *Methods Mol Biol* 490:83–113.
30. Philo JS (2006) Improved methods for fitting sedimentation coefficient distributions derived by time-derivative techniques. *Anal Biochem* 354:238–246.
31. Erickson HP (2009) Size and shape of protein molecules at the nanometer level determined by sedimentation, gel filtration, and electron microscopy. *Biol Proced Online* 11:32–51.
32. Climent I, Sjöberg B-M, Huang CY (1992) Site-directed mutagenesis and deletion of the carboxyl terminus of Escherichia coli ribonucleotide reductase protein R2. Effects on catalytic activity and subunit interaction. *Biochemistry* 31:4801–4807.
33. Svergun DaK M (2003) Small-angle scattering studies of biological macromolecules in solution. *Rep Prog Phys* 66:1735–1782.
34. Ormo M, Sjöberg B-M (1990) An ultrafiltration assay for nucleotide binding to ribonucleotide reductase. *Anal Biochem* 189:138–141.
35. Segel DJ, Fink AL, Hodgson KO, Doniach S (1998) Protein denaturation: A small-angle X-ray scattering study of the ensemble of unfolded states of cytochrome c. *Biochemistry* 37:12443–12451.
36. Putnam CD, Hammel M, Hura GL, Tainer JA (2007) X-ray solution scattering (SAXS) combined with crystallography and computation: Defining accurate macromolecular structures, conformations and assemblies in solution. *Q Rev Biophys* 40:191–285.
37. Mylonas E, Svergun DI (2007) Accuracy of molecular mass determination of proteins in solution by small-angle X-ray scattering. *J Appl Crystallogr* 40:s245–s249.
38. Uppsten M, Farnegardh M, Domkin V, Uhlin U (2006) The first holocomplex structure of ribonucleotide reductase gives new insight into its mechanism of action. *J Mol Biol* 359:365–377.
39. Nordlund P, Sjöberg B-M, Eklund H (1990) Three-dimensional structure of the free radical protein of ribonucleotide reductase. *Nature* 345:593–598.
40. Salowe SP, Stubbe J (1986) Cloning, overproduction, and purification of the B2 subunit of ribonucleoside-diphosphate reductase. *J Bacteriol* 165:363–366.
41. Salowe SP, Ator MA, Stubbe J (1987) Products of the inactivation of ribonucleoside diphosphate reductase from Escherichia coli with 2′-azido-2′-deoxyuridine 5′-diphosphate. *Biochemistry* 26:3408–3416.
42. Hogbom M, et al. (2003) Displacement of the tyrosyl radical cofactor in ribonucleotide reductase obtained by single-crystal high-field EPR and 1.4-angstrom X-ray data. *Proc Natl Acad Sci USA* 100:3209–3214.
43. Ando N, Chenevier P, Novak M, Tate MW, Gruner SM (2008) High hydrostatic pressure small-angle X-ray scattering cell for protein solution studies featuring diamond windows and disposable sample cells. *J Appl Crystallogr* 41:167–175.
44. Konarev PV, Petoukhov MV, Volkov VV, Svergun DI (2006) ATSAS 2.1, a program package for small-angle scattering data analysis. *J Appl Crystallogr* 39:277–286.
45. Schuck P (2000) Size-distribution analysis of macromolecules by sedimentation velocity ultracentrifugation and lamm equation modeling. *Biophys J* 78:1606–1619.
46. Laue TM, Shah BD, Ridgeway TM, Pelletier SL (1992) Computer-aided interpretation of analytical sedimentation data for proteins. *Analytical Ultracentrifugation in Biochemistry and Polymer Science*, eds SE Harding et al. (Royal Soc Chemistry, Cambridge, UK), pp 90–125.
47. Garcia de la Torre J (2001) Building hydrodynamic bead-shell models for rigid bioparticles of arbitrary shape. *Biophys Chem* 94:265–274.
48. Tang G, et al. (2007) EMAN2: An extensible image processing suite for electron microscopy. *J Struct Biol* 157:38–46.
49. Voss NR, Yoshioka CK, Radermacher M, Potter CS, Carragher B (2009) DoG Picker and TiltPicker: software tools to facilitate particle selection in single particle electron microscopy. *J Struct Biol* 166:205–213.
50. Brignole EJ, Smith S, Asturias FJ (2009) Conformational flexibility of metazoan fatty acid synthase enables catalysis. *Nat Struct Mol Biol* 16:190–197.
51. von Dobeln U, Reichard P (1976) Binding of substrates to Escherichia coli ribonucleotide reductase. *J Biol Chem* 251:3616–3622.